

## ECOLOGY

# Critical soil moisture thresholds of plant water stress in terrestrial ecosystems

Zheng Fu<sup>1\*</sup>, Philippe Ciais<sup>1</sup>, Andrew F. Feldman<sup>2</sup>, Pierre Gentine<sup>3</sup>, David Makowski<sup>4</sup>, I. Colin Prentice<sup>5,6</sup>, Paul C. Stoy<sup>7</sup>, Ana Bastos<sup>8</sup>, Jean-Pierre Wigneron<sup>9</sup>

Plant water stress occurs at the point when soil moisture (SM) limits transpiration, defining a critical SM threshold ( $\theta_{crit}$ ). Knowledge of the spatial distribution of  $\theta_{crit}$  is crucial for future projections of climate and water resources. Here, we use global eddy covariance observations to quantify  $\theta_{crit}$  and evaporative fraction (EF) regimes. Three canonical variables describe how EF is controlled by SM: the maximum EF ( $EF_{max}$ ),  $\theta_{crit}$ , and slope (S) between EF and SM. We find systematic differences of these three variables across biomes. Variation in  $\theta_{crit}$ , S, and  $EF_{max}$  is mostly explained by soil texture, vapor pressure deficit, and precipitation, respectively, as well as vegetation structure. Dryland ecosystems tend to operate at low  $\theta_{crit}$  and show adaptation to water deficits. The negative relationship between  $\theta_{crit}$  and S indicates that dryland ecosystems minimize  $\theta_{crit}$  through mechanisms of sustained SM extraction and transport by xylem. Our results further suggest an optimal adaptation of local EF-SM response that maximizes growing-season evapotranspiration and photosynthesis.

## INTRODUCTION

The critical soil moisture (SM) threshold ( $\theta_{crit}$ ) of plant water stress occurs near the point when evapotranspiration becomes SM-limited (1). Below this threshold, a marginal reduction of SM leads to reduced evapotranspiration and increased sensible heat flux (2). Crossing this threshold results into decreased evaporative fraction (EF), the ratio of latent heat to the sum of latent and sensible heat fluxes, making the air above the canopy warmer and drier, which, in turn, further reduces transpiration and plant carbon dioxide uptake (3–5). The existence of critical SM thresholds plays a crucial role in the surface energy partitioning (6–8). SM-controlled energy partitioning determines local climate and land-atmosphere coupling and can amplify warming in transition regions (9, 10). A better knowledge of critical SM thresholds is also important to assess crop yield risks and ecosystem vulnerability from drought exposure (7).

The land surface hydrology community has historically observed that the  $\theta_{crit}$  level at which water limitation of evapotranspiration begins is above the SM wilting point of extreme stress (7). However, it is not clear whether plant photosynthetic processes become water-stressed at the same  $\theta_{crit}$  as evapotranspiration. For evapotranspiration, the  $\theta_{crit}$  can be quantified by evaluating the EF-SM relationship (2, 5, 8, 11, 12). For photosynthesis, the onset of water stress at ecosystem level was found to correspond to the SM critical value at which the sign of the covariance between daily gross primary production (GPP) and vapor pressure deficit (VPD) switches from a

positive to negative sign when SM decreases during a soil drying period (13). GPP and evapotranspiration are tightly coupled on short time scales (4), and VPD combines the effects of both water stress and energy demand (via temperature) on GPP (14–16). Comparing  $\theta_{crit}$  values diagnosed from the covariance of GPP and VPD (the “VPD-GPP-SM method”) with those calculated from EF-SM relationships (the “EF-SM method”) can help us understand whether evapotranspiration and photosynthetic processes become water-limited under similar SM conditions.

The relationship between EF and SM shows two regimes: energy-limited and water-limited evapotranspiration (2, 5, 11, 12). When SM is higher than  $\theta_{crit}$ , the system is energy-limited, as less SM does not necessarily lead to lower evapotranspiration (17, 18). Evapotranspiration is at or near its potential value when net radiation is limiting, and EF stays near a maximum value ( $EF_{max}$ ). In contrast, when SM is lower than  $\theta_{crit}$ , the capacity of plants to extract soil water by roots and xylem transport becomes progressively reduced. Under this SM-limited regime, evapotranspiration decreases with decreasing SM until the wilting point, where transpiration is blocked because of full stomatal closure, with little or no further change in EF with SM decrease (8). In the SM-limited regime, EF decreases with decreasing SM, and this decrease is approximately linear (8, 12, 19). The SM regime can self-amplify itself because a lower evapotranspiration increases surface temperature and VPD and prevents the formation of boundary layer clouds (3, 20). These feedbacks further increase net radiation and atmospheric dryness at larger scales, which accelerates the depletion of SM, causing a positive “dry gets dryer” land-atmosphere climate feedback (4, 5, 21).

The relationship between EF and SM can thus be summarized by three parameters: a constant  $EF_{max}$  in the energy-limited regime, the  $\theta_{crit}$  breaking point at which EF decreases with SM, and the linear slope (S) between EF and SM below this breaking point. This EF-SM framework is conceptually well established, but quantifying  $\theta_{crit}$  to delineate the transition from energy to water-limited regimes across biomes and climate zones has been mainly limited to model-based studies due to a lack of observations (11, 18, 22, 23). At the global scale, so far, there is no observation-based assessment of  $\theta_{crit}$ , S, and  $EF_{max}$ , although few studies reported some of them at sites or regional

<sup>1</sup>Laboratoire des Sciences du Climat et de l'Environnement, LSCE/IPSL, CEA-CNRS-UVSQ, Université Paris-Saclay, 91191 Gif-sur-Yvette, France. <sup>2</sup>NASA Goddard Space Flight Center, Earth Sciences Division, Greenbelt, MD 20771, USA. <sup>3</sup>Department of Earth and Environmental Engineering, Columbia University, New York, NY 10027, USA. <sup>4</sup>Unit Applied Mathematics and Computer Science (UMR 518), INRAE, AgroParisTech, Université Paris-Saclay, Paris, France. <sup>5</sup>Georgina Mace Centre for the Living Planet, Department of Life Sciences, Imperial College London, Silwood Park Campus, Buckhurst Road, Ascot SL5 7PY, UK. <sup>6</sup>Ministry of Education Key Laboratory for Earth System Modeling, Department of Earth System Science, Tsinghua University, Beijing 100084, China. <sup>7</sup>Department of Biological Systems Engineering, University of Wisconsin-Madison, Madison, WI 53706, USA. <sup>8</sup>Department Biogeochemical Integration, Max Planck Institute for Biogeochemistry, D-07745 Jena, Germany. <sup>9</sup>ISPA, INRAE, Université de Bordeaux, Bordeaux Sciences Agro, F-33140 Villenave d'Ornon, France. \*Corresponding author. Email: zheng.fu@lsce.ipsl.fr

scales (13, 18, 22). Even less is known about the mechanisms that control the three parameters of the EF-SM relationship. Earth system models include parametric functional SM–evaporation relationships, with parameters set to ad hoc values and kept constant in space and time (24). Differences in parameter values and functional relationships across models is a key source of divergence and uncertainty in their water and carbon cycle projections (6, 18, 25). Dirmeyer *et al.* (25) reported that an ensemble of models had no consistent representation of the connection between EF and SM. Quantifying the parameters of  $\theta_{\text{crit}}$ ,  $S$ , and  $EF_{\text{max}}$  and their drivers across biomes and climates is therefore critical to identify the mechanisms of water stress tipping points and improve models to predict future climate accurately.

To quantify  $\theta_{\text{crit}}$  directly, we used accurate and high-frequency measurements of EF from eddy covariance flux towers during extensive periods without rainfall, when a transition from energy to water limitation is likely to happen. These periods during when SM decreases are known as dry-downs (18, 26, 27). From a systematic analysis of multiple dry-downs, we derive the EF-SM relationship and  $\theta_{\text{crit}}$  using daily latent and sensible heat flux observations from each site of the global network of flux tower measurements (see Materials and Methods). The objectives of this study are (i) to quantify the three parameters  $\theta_{\text{crit}}$ ,  $S$ , and  $EF_{\text{max}}$  of the EF-SM relationship across diverse plant functional groups and climate types; (ii) to examine the climatic, biotic, and edaphic predictors that control the spatial variability of  $\theta_{\text{crit}}$ ,  $S$ , and  $EF_{\text{max}}$ ; and (iii) to investigate the consistency of  $\theta_{\text{crit}}$  derived from the EF-SM and VPD-GPP-SM methods globally to determine whether evapotranspiration and photosynthetic processes become water-limited under similar SM conditions. On the basis of these results, we then evaluate possible relationships between the parameters and test whether the observed varying responses of EF-SM can be explained by an optimality principle.

## RESULTS

### Consistency of $\theta_{\text{crit}}$ derived from the EF-SM and VPD-GPP-SM methods

During a dry-down, EF remains relatively steady at first (energy-limited evapotranspiration stage) but then decreases when surface SM (volumetric soil water content; see Materials and Methods) becomes lower than a given threshold. Figure 1A shows this behavior at a forest site in Germany, DE-Hzd (table S1). The EF-SM relationship is characterized by the  $\theta_{\text{crit}}$  transition point in SM, separating the water and energy-limited regimes. Using eight dry-downs recorded during two peak growing seasons, we find that surface  $\theta_{\text{crit}}$  for EF is equal to  $23.4 \pm 0.5\%$  at this site (Fig. 1B). From the change in sign of the covariance between daily VPD and GPP (Fig. 1C), we find that surface  $\theta_{\text{crit}}$  for GPP has a value of 24.5%, which is very close to the EF-based estimate. Thus,  $\theta_{\text{crit}}$  values estimated for EF and GPP at this site are very similar.

Next, we systematically compared the two  $\theta_{\text{crit}}$  values estimated from EF and GPP. Across all sites, the two methods give consistent results [correlation coefficient ( $r$ ) = 0.82; Fig. 1D], suggesting that EF and GPP both become water-limited under similar SM conditions. Thus, the EF-SM relationship during dry-downs is an effective method to quantify the SM threshold of plant water stress, despite the fact that EF is also affected by changes in bare soil evaporation, which is partly decoupled from the water stress on transpiration and GPP. A second point is that the VPD-GPP-SM method originally proposed

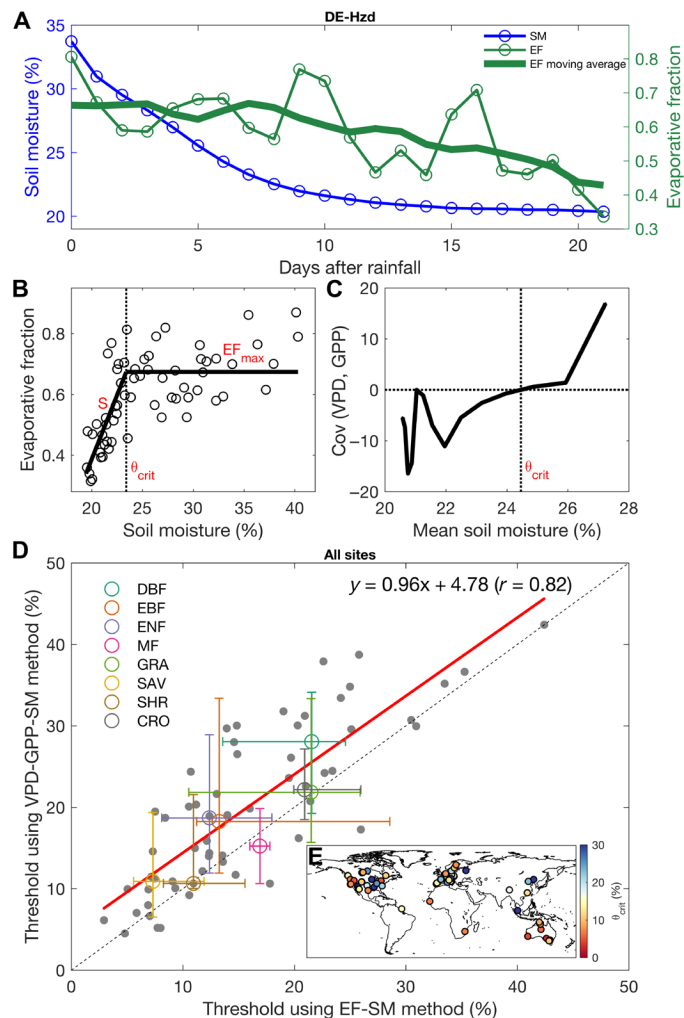


**Fig. 1. Quantifying the critical SM threshold during SM dry-downs using the EF-SM method and the VPD-GPP-SM method.** SM and EF changes during a dry-down at a forest site, DE-Hzd (A). Estimating SM threshold from the EF-SM method (B) and the VPD-GPP-SM method (C) using all dry-downs at DE-Hzd. Comparison between the SM thresholds estimated from the VPD-GPP-SM method and the EF-SM method across all sites (D). Median and the 25th and 75th percentiles are shown for each biome. The dashed line is the 1:1 line. Covariance and mean SM were calculated using a 9-day moving window (e.g., 1 to 9 days, 2 to 10 days, and 3 to 11 days) following Fu *et al.* (13). The units of covariance between VPD and GPP are micromoles of  $\text{CO}_2$  per square meter per second hectopascal. Map of the flux tower sites used in this analysis (E). Colors indicate the  $\theta_{\text{crit}}$  values using EF-SM method. EBF, evergreen broadleaf forests; ENF, evergreen needleleaf forests; MF, mixed forests; GRA, grasslands; SAV, savannas; SHR, shrublands; CRO, croplands.

for European ecosystems works globally, extending previous results from Fu *et al.* (13). Because the VPD-GPP-SM method requires longer dry-down periods to calculate the covariance between daily VPD and GPP, the EF-SM method was retained for this study involving a large numbers of sites on a global scale (Fig. 1E). We systematically calculated the three parameters that fully explain the EF-SM relationship at each site, as shown in Fig. 1B, namely,  $EF_{\text{max}}$  during the first part of the dry-downs in the absence of water stress,  $\theta_{\text{crit}}$  for the inception of the EF decrease with SM, and the  $S$  of the linear relationship between EF and SM below  $\theta_{\text{crit}}$ , when water stress intensifies.

**$\theta_{crit}$ , S, and  $EF_{max}$  among biomes and climate zones**

We find that the  $\theta_{crit}$  diagnosed from recurrent dry-downs of surface SM is highly correlated with the  $\theta_{crit}$  estimated from deeper SM (fig. S3). As surface SM measurements are available at all sites, we focus on surface SM. Across all sites globally, we find that the median  $\theta_{crit}$ , S, and  $EF_{max}$  are  $14.0 \pm 0.9\%$  ( $\pm SE$ ),  $0.045 \pm 0.005$ , and  $0.57 \pm 0.02$ , respectively (fig. S4). These three canonical parameters have notably large spatial variations, suggesting differences in behavior across biomes and climate zones (Fig. 2). The value of  $\theta_{crit}$  in savannas ( $7.2 \pm 1.1\%$ ) is much lower than in deciduous broadleaf forests (DBFs;  $19.7 \pm 2.4\%$ ), grasslands ( $21.4 \pm 2.4\%$ ), and croplands ( $20.9 \pm 2.5\%$ ; Fig. 2A). Ecosystems in temperate ( $18.8 \pm 1.3\%$ ), continental ( $17.1 \pm 3.3\%$ ), and subtropical climates ( $14.7 \pm 1.7\%$ ) have higher  $\theta_{crit}$  values than in dry climates ( $7.0 \pm 1.1\%$ ; Fig. 2B). The S value in savannas ( $0.082 \pm 0.019$ ) is three times higher than in grasslands ( $0.026 \pm 0.009$ ; Fig. 2C). Sites in temperate climates ( $0.033 \pm 0.005$ ) have lower S values than dry climates ( $0.090 \pm 0.025$ ; Fig. 2D). Regarding  $EF_{max}$ , the high values are mainly in croplands ( $0.78 \pm 0.04$ ), grasslands ( $0.67 \pm 0.02$ ), and DBFs ( $0.63 \pm 0.02$ ), and they are significantly larger than in evergreen needleleaf forests ( $0.45 \pm 0.02$ ; Fig. 2E). Boreal climates ( $0.43 \pm 0.04$ ) have smaller  $EF_{max}$  values than tropical climates ( $0.71 \pm 0.03$ ; Fig. 2F). Combining biomes and

climate types, the values of  $\theta_{crit}$ , S, and  $EF_{max}$  also vary among different ecosystems (fig. S5), although statistical testing of these differences is impractical because of the limited sample size in each bin. We also find that variations of the three parameters  $\theta_{crit}$ , S, and  $EF_{max}$  are substantial within any one biome or climate zone (Fig. 2), implying the existence of other local controlling factors.

**Drivers of the spatial variability of  $\theta_{crit}$ , S, and  $EF_{max}$** 

We analyze the relative importance of soil texture (sand fraction), vegetation structural characteristics [approximated by maximum leaf area index ( $LAI_{max}$ )], and mean climatic variables (mean VPD and total precipitation during peak growing season) on the spatial variability of  $\theta_{crit}$ , S, and  $EF_{max}$  using random forests (see Materials and Methods). The cross-validation shows that these predictors explain 43, 46, and 38% of the spatial variability of  $\theta_{crit}$ , S, and  $EF_{max}$ , respectively. The dominant predictors of the spatial variability of  $\theta_{crit}$ , S, and  $EF_{max}$  were, however, different. We find that the spatial variability of  $\theta_{crit}$  is mostly explained by the sand fraction and  $LAI_{max}$  (Fig. 3A), while the spatial variability of S is mainly explained by VPD and  $LAI_{max}$  (Fig. 3F). The spatial variability of  $EF_{max}$  is mostly explained by precipitation amount, followed by  $LAI_{max}$  (Fig. 3K). Partial dependence analysis confirms that  $\theta_{crit}$  across sites is reduced

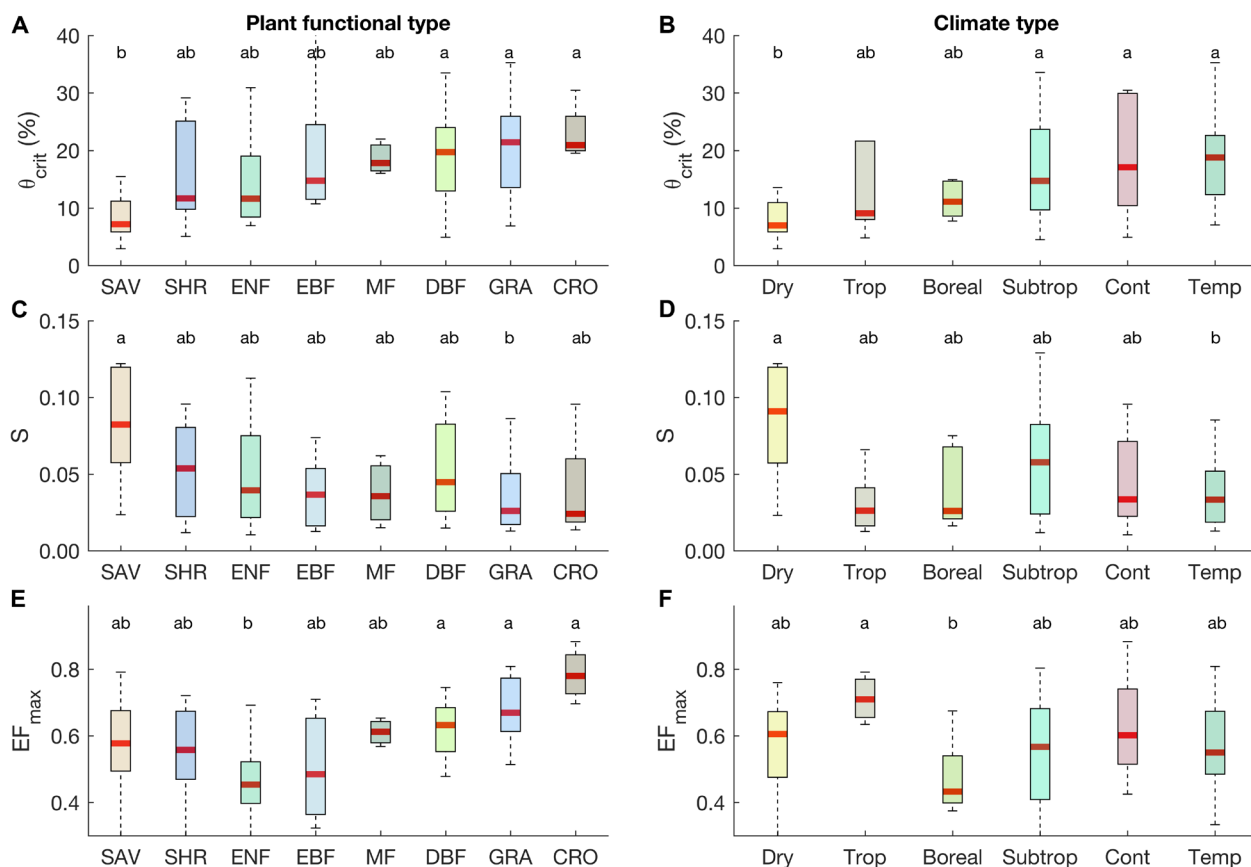


**Fig. 2.**  $\theta_{crit}$ , S, and  $EF_{max}$  among different plant functional types and climate types.  $\theta_{crit}$  (A and B), S (C and D), and  $EF_{max}$  (E and F) among different plant functional types (A, C, and E) and climate types (B, D, and F). Letters represent statistically significant differences in the median values (Kruskal-Wallis test,  $P < 0.05$ ), such that groups not containing the same letter are different. For each box plot, the middle line indicates the median; the box indicates the upper and lower quartiles and the whiskers indicate the 5th and 95th percentiles of the data. Plant functional types were defined according to the International Geosphere-Biosphere Programme classification, including SAV, SHR, ENF, EBF, DBF, MF, GRA, and CRO. Climate types were defined according to the Köppen-Geiger classification as in Migliavacca *et al.* (65): tropical (Aw, Af, and Am), dry (BSh, BSk, and BWh), subtropical (Cfa, Csa, Csb, and Cwa), temperate (Cfb), continental (Dfa, Dfb, Dwa, Dw, and Dwc), and boreal (Dfc and Dsc).

considerably with a higher sand fraction (Fig. 3B) but increased with  $LAI_{max}$  (Fig. 3C). In addition,  $\theta_{crit}$  shows a positive dependence on precipitation (Fig. 3D) and a negative dependence on VPD (Fig. 3E). In contrast,  $S$  increases greatly with higher VPD (Fig. 3J) but decreases with increasing  $LAI_{max}$  (Fig. 3H).  $S$  is also less steep at higher precipitation (Fig. 3I) and for soils with a lower sand fraction (Fig. 3G). The opposite responses of  $\theta_{crit}$  and  $S$  to all these four environmental factors (Fig. 3, B to E and G to J) indicate that there is a negative relationship between  $\theta_{crit}$  and  $S$  (see later). For  $EF_{max}$ , we find that increasing precipitation and  $LAI_{max}$  mainly enhances  $EF_{max}$  (Fig. 3, M and N), while  $EF_{max}$  decreases with increasing sand fraction (Fig. 3L).

### Relationships between $\theta_{crit}$ , $S$ , and $EF_{max}$ and the optimal adaptation of local EF-SM responses

Across all sites, we find that  $\theta_{crit}$  exhibits a significant negative correlation with  $S$  and a positive correlation with  $EF_{max}$  (Fig. 4A). This is further confirmed by partial correlation analysis (Fig. 4B). Thus, there is a trade-off between  $\theta_{crit}$  and  $S$ : Sites with low  $\theta_{crit}$  often have high  $S$  values, while sites with high  $\theta_{crit}$  often have low  $S$  values (Fig. 4, A and B). To understand the negative relationship between  $\theta_{crit}$  and  $S$ , we define the intersection of the fitted segmented curve with the  $x$  axis at each site as  $\theta_0$  (see Materials and Methods). Across sites, the value of  $\theta_0$  does not significantly differ from zero (fig. S7).

The  $S$  values in different biomes can therefore be predicted using the ratio of  $EF_{max}$  and  $\theta_{crit}$  (fig. S8). The relationships between  $\theta_{crit}$ ,  $S$ , and  $EF_{max}$  can be related to the dryness of the climate. We thus calculated the aridity index (AI), defined as the ratio of annual potential evapotranspiration (PET) to annual precipitation, from the eddy covariance measurements at each site (see Materials and Methods). We find that low  $\theta_{crit}$  and high  $S$  values are more common in dry sites (AI > 4), while high  $\theta_{crit}$  and low  $S$  values are more common in wet sites (AI < 3; fig. S9).

The distribution of  $\theta_{crit}$  and  $S$  across different biomes leads us to hypothesize two strategies for how ecosystem has adapted to prevailing recurrent water stress: (i) low  $\theta_{crit}$  with high  $S$  (e.g., savannas) and (ii) high  $\theta_{crit}$  with low  $S$  [e.g., grasslands (mainly in temperate and continental climates)] (Figs. 2, A and C, and 4A). The first strategy reflects a resistance to soil dryness and is more successful for ecosystems experiencing frequent dry-downs. However, below the infrequently reached  $\theta_{crit}$  value, transpiration and ecosystem function may collapse rapidly. The second strategy, which consists in having a high  $EF_{max}$  and a high  $\theta_{crit}$  is better adapted to humid and subhumid environments where dry-downs are shorter, less severe, and less frequent, so that the number of days with SM below  $\theta_{crit}$  is low, and ecosystems can maximize  $EF_{max}$  to sustain water use for photosynthesis.

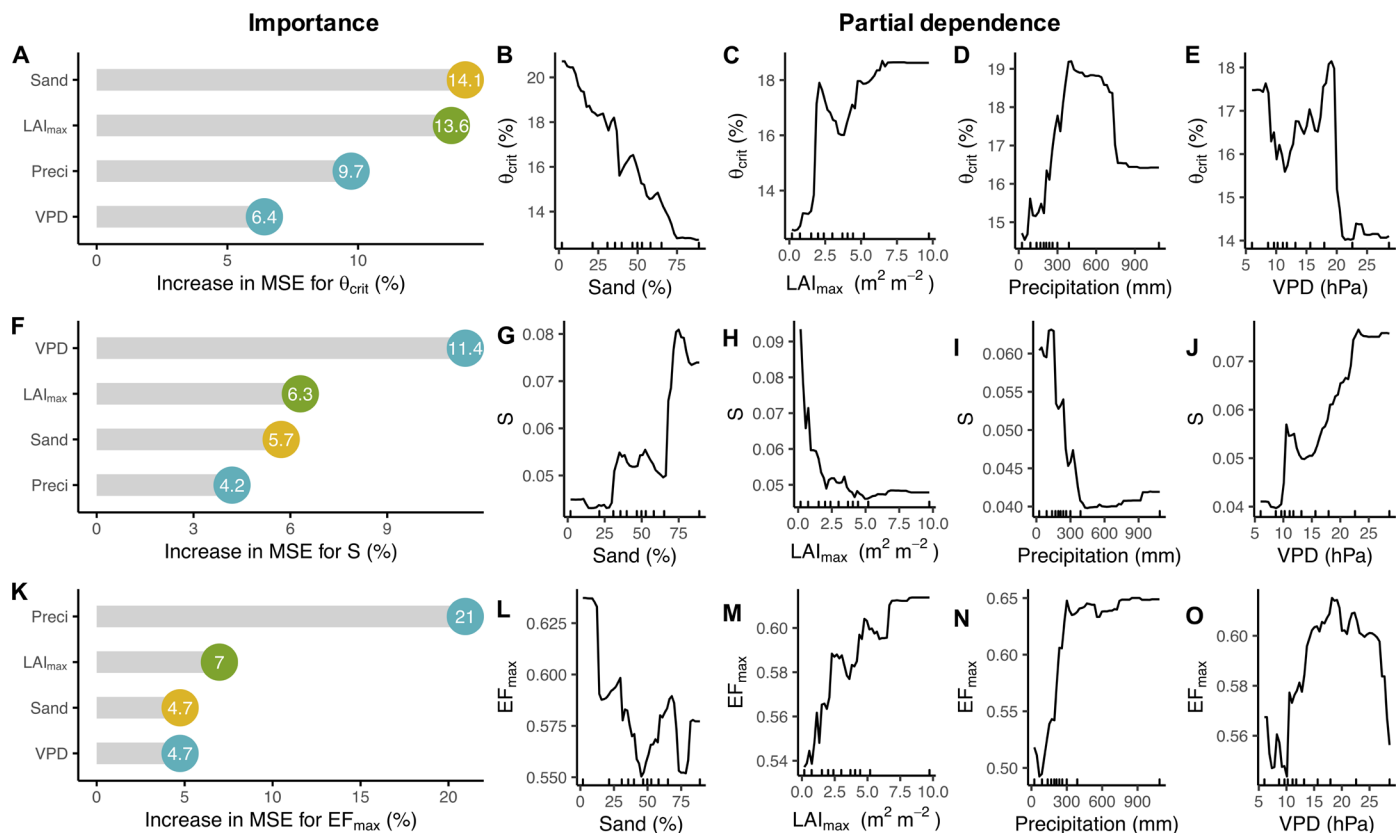


**Fig. 3. Importance of soil, vegetation structure, and climate properties and partial dependence.** Predictive relative importance for  $\theta_{crit}$  (A),  $S$  (F), and  $EF_{max}$  (K). Numbers in the circles represent the percentage increase in mean squared error (MSE). Yellow circles represent soil variable; green circles represent vegetation structure variable; light blue circles represent climate variables. Partial dependence plots indicate the sensitivity of the response variable to the specific predictor. Sand, sand fraction (%);  $LAI_{max}$ , maximum leaf area index (in square meters per square meter); VPD, mean VPD during the peak growing season (in hectopascals); Preci, total precipitation amount during the peak growing season (in millimeters). Tick marks in the x axis represent the minimum, maximum, and deciles of the variable distribution.



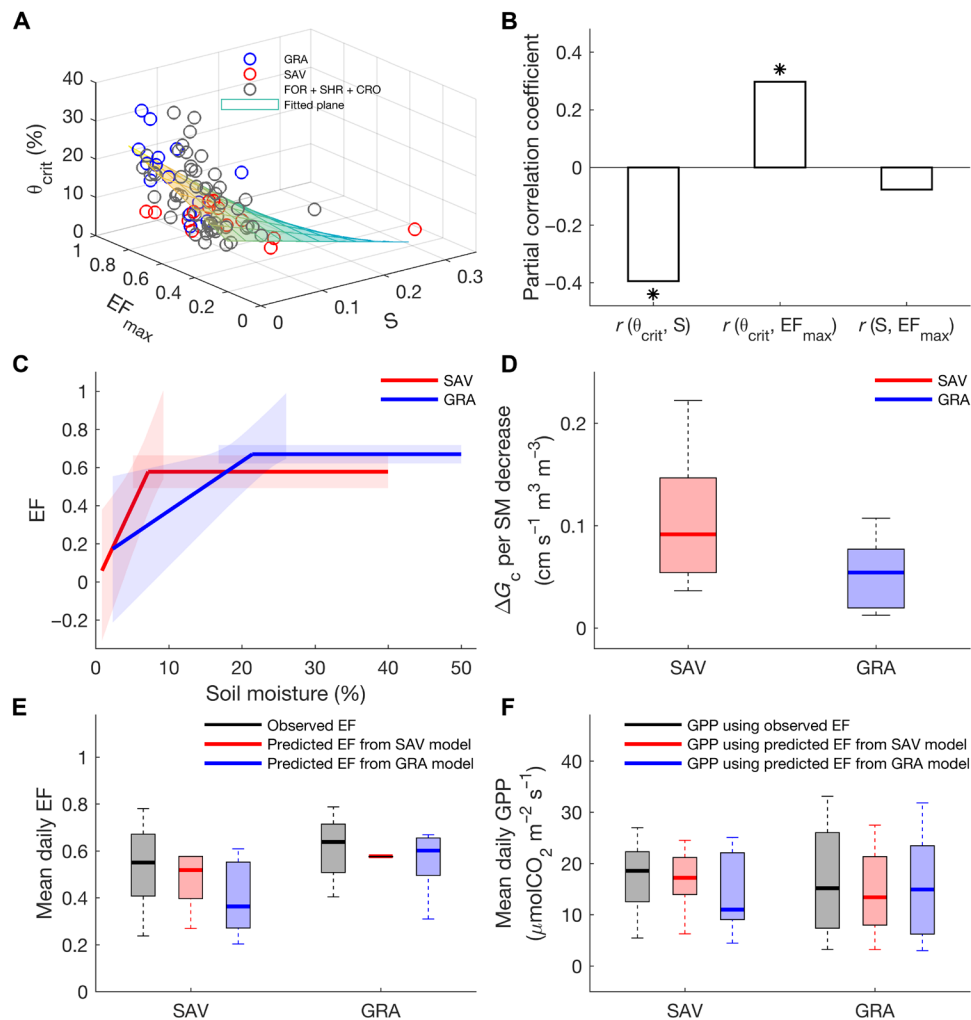


**Fig. 4. Relationships between  $\theta_{\text{crit}}$ ,  $S$ , and  $EF_{\text{max}}$  and the optimal adaptation of local EF-SM response function.** The distribution of  $\theta_{\text{crit}}$ ,  $S$ , and  $EF_{\text{max}}$  across all sites in different biomes (A). Partial correlation between  $\theta_{\text{crit}}$ ,  $S$ , and  $EF_{\text{max}}$  across all sites (B). \* $P < 0.05$ . The mean response functions of EF-SM in savannas and grasslands (C), while the shading bounds the 95% confidence interval. The canopy conductance ( $G_c$ ) change rates per SM decrease during water-limited stage in savannas and grasslands (D). Observed and predicted mean daily EF during the peak growing season in savannas and grasslands by swapping two response functions of EF-SM: one from savannas and one from grasslands (E). Calculated mean daily GPP during the peak growing season in savannas and grasslands using observed and predicted EF from two response functions of EF-SM (F). For each box plot, the middle line indicates the median; the box indicates the upper and lower quartiles, and the whiskers indicate the 5th and 95th percentiles of the data.

As both  $\theta_{\text{crit}}$  and  $S$  values are significantly different between savannas and grasslands (Fig. 2, A and C), the response functions of EF-SM in these two biomes are further compared (see Materials and Methods). We find that the response curve of mean EF-SM in savannas and grasslands is in line with the general results observed across sites; namely,  $\theta_{\text{crit}}$  is negatively related to  $S$  but positively related to  $EF_{\text{max}}$  (Fig. 4, A to C). The higher  $S$  value found in savannas implies that canopy conductance ( $G_c$ ) may be reduced more strongly when SM passes below  $\theta_{\text{crit}}$ , while the lower  $S$  value in grasslands indicates that  $G_c$  may decrease more progressively when SM unfrequently gets below  $\theta_{\text{crit}}$ . To test this hypothesis, we calculated the reduction rate of  $G_c$  with decreasing SM under the water-limited stage in these two biomes, respectively (see Materials and Methods). We find that the reduction rate of  $G_c$  with SM in savannas ( $9 \pm 2 \text{ cm s}^{-1} \text{ m}^3 \text{ m}^{-3}$ ) is significantly larger than in grasslands ( $5 \pm 1 \text{ cm s}^{-1} \text{ m}^3 \text{ m}^{-3}$ ; Fig. 4D). Thus, the higher  $S$  values in savannas correspond

to a stronger stomatal closure in response to an SM decrease under water-limited conditions to prevent hydraulic failure. In contrast, the lower  $S$  values in grasslands imply a more gradual stomatal closure in response to SM decrease, favoring photosynthesis in periods of low to moderate water stress.

We formulated a second hypothesis that the contrasted response functions of EF-SM between savannas (low  $\theta_{\text{crit}}$  and high  $S$ ) and grasslands (high  $\theta_{\text{crit}}$  and low  $S$ ) locally maximize growing-season evapotranspiration and EF. To test this, we predicted the mean daily EF during the peak growing season for each site in savannas and grasslands by exchanging the two responses of EF-SM (from savannas to grasslands and vice versa) (see Materials and Methods). Comparing with observed and predicted mean daily EF using the true EF-SM response, we find that the predicted mean daily EF using the EF-SM response curve from the other biome is underestimated (Fig. 4E). This finding suggests that EF-SM response curves are adapted so as

to maximize growing-season EF. To further test whether maximizing EF also implies maximization of photosynthesis during the peak growing season, we performed the same analysis for GPP (see Materials and Methods). We find that, in both savannas and grasslands, the predicted mean growing-season GPP using the EF-SM model of the other biome is always lower than the predicted GPP using the true EF-SM model (Fig. 4F). Thus, our results show that the trade-off between  $\theta_{\text{crit}}$  and  $S$  helps to maximize the growing-season EF and the optimal adaptation of the local EF-SM response function of the ecosystem can maximize growing-season evapotranspiration and photosynthesis. Except for savannas and grasslands, we could not compare the response functions of EF-SM among other biomes (forests, shrublands, and croplands) because they do not have significant differences in either  $\theta_{\text{crit}}$  or  $S$  (Fig. 2, A and C).

## DISCUSSION

Vegetation regulates the terrestrial water and carbon cycles, as it controls and adapts to changing SM availability. However, our ability to characterize the  $\theta_{\text{crit}}$  at the global scale is limited. By examining the consistency of  $\theta_{\text{crit}}$  estimated from the VPD-GPP-SM and EF-SM methods, this study showed that plant photosynthetic processes become water-stressed at an SM threshold similar to that of EF, suggesting that the EF-SM relationship is able to quantify the SM threshold of plant water stress. We noted that the absolute magnitudes of  $\theta_{\text{crit}}$  values estimated from the VPD-GPP-SM method are slightly higher than those from the EF-SM method (Fig. 1D). This higher value is likely due to the fact that the VPD-GPP covariance is calculated using a 9-day moving window that, therefore, can overestimate the threshold during dry-downs (13). Meanwhile, this bias may be also related to the bias in GPP for different flux tower sites due to the inhibition of leaf respiration in the light (28) and uncertainty in the gap-filling routine. The uncertainty in tower-estimated GPP depends, in part, on radiation, which would affect the SM thresholds estimated from VPD-GPP-SM method for different sites. Nevertheless, the relatively small mean difference but strong spatial correlation between the two thresholds across all sites and all biomes shows that SM limitation occurs at a similar SM level for GPP and evapotranspiration. This EF-SM approach used here also provided a practical application of the original conceptual Budyko curve (11) yet based on a temporal approach rather than spatial approach. The Budyko framework is commonly used to estimate the long-term mean actual evaporation as a function of the mean AI at the catchment scale and applied as a spatial analysis for mean evapotranspiration/precipitation (29). We focused here on the transient shift between energy and water limitations at the site scale (and at short time scales) and used SM to quantify ecosystem water limitation.

Land-surface models typically represent SM stress effects on evapotranspiration and GPP as a segmented function (30), consistent with our empirical analysis. Some models set  $\theta_{\text{crit}}$  at field capacity; then, at lower SM, evapotranspiration and GPP are multiplied by a moisture scalar, which declines either linearly or nonlinearly from 1 at field capacity to 0 at wilting point (30). Our results suggest that a linear formula with  $\theta_{\text{crit}}$  set to field capacity will overestimate water stress. Other models more realistically define a  $\theta_{\text{crit}}$  that is less than field capacity and greater than the wilting point (31). In addition, a moisture scalar is also used in some satellite GPP and evapotranspiration algorithms. For example, satellite-driven light use efficiency (LUE) GPP models used environmental scalars to represent biophysical

constraints on maximum LUE (32, 33), but many of the existing and widely used LUE models do not currently incorporate SM constraints directly (34). Our study provides an SM stress framework and parameterization that could be incorporated in the future to improve these models. The formulation introduced in this study is also compatible with formulations already used in light-use efficiency and process-based land surface models, but the three parameter values here are based on analysis of measured data, providing observations of key parameters of the SM control on evapotranspiration. The  $\theta_{\text{crit}}$  value that we found is in line with the value found in the Netherlands (16%) (35) and Africa (14%) (18) using satellite observations, while our estimates of  $S$  and  $\text{EF}_{\text{max}}$  across sites are slightly higher than the values reported in Europe ( $S = 0.03$  and  $\text{EF}_{\text{max}} = 0.54$ ) (13). We also found that there are large and systematic differences in these three parameters across biomes and climate zones. Even within a given plant functional type or climate type, the spatial variations in  $\theta_{\text{crit}}$ ,  $S$ , and  $\text{EF}_{\text{max}}$  are also large. Thus, it is unrealistic to parameterize these variables as universal constants, similar to those in many models. Although models simulate SM in different layers, whereas our analysis was based on surface observations, our results demonstrate that the surface  $\theta_{\text{crit}}$  is highly correlated with the  $\theta_{\text{crit}}$  in deep soil layers (fig. S3), which is consistent with the recent findings that surface and rootzone SM are equivalently skillful for identifying evapotranspiration regime changes (36). We also found that, when surface  $\theta_{\text{crit}}$  is larger than 20%,  $\theta_{\text{crit}}$  based on SM dry-downs of the deep soil layers is higher than surface  $\theta_{\text{crit}}$  (fig. S3). This may be because the deep SM is relatively stable and acts as a low-pass filter so that it will not be depleted as efficiently by plant roots compared with surface SM.

In addition to helping improve the representation of water stress in models, eddy covariance observations from globally distributed and automated sensor networks analyzed here with a machine learning approach also unravel previously unidentified relationships between parameter values and environmental variables. Our results showed that the spatial variability of  $\theta_{\text{crit}}$ ,  $S$ , and  $\text{EF}_{\text{max}}$  is mostly explained by soil texture, mean growing-season VPD, and precipitation, respectively, while  $\text{LAI}_{\text{max}}$  also affects their values. The variability of  $\theta_{\text{crit}}$  is dominantly explained by the sand fraction, consistent with lower wilting points observed in sandy soils (37). Plant water stress is related to water potential, which largely is affected by the soil capacity to hold water (38, 39). Sandy soils have greater hydraulic conductivity and lower porosity than other soil types (e.g., clay) (40, 41); thus, there is a lower soil water holding capacity in sandy soils. The spatial variability of  $S$  is mainly explained by VPD, while the spatial variability of  $\text{EF}_{\text{max}}$  is mostly explained by the precipitation amount. Increasing VPD triggers stomatal closure (14) and reduces transpiration and EF, thus increasing  $S$ .  $\text{LAI}_{\text{max}}$  has important contributions to the spatial variability of all these three parameters, highlighting the critical role of vegetation structure in controlling evapotranspiration processes. This result is in keeping with a previous study from Williams and Torn (42), showing that LAI controls surface heat flux partitioning and land-atmosphere coupling. As they have a lower  $\text{LAI}_{\text{max}}$  and grow on more sandy soils (fig. S10), savannas have lower  $\theta_{\text{crit}}$  and higher  $S$  than that of grasslands. Grasslands also tend to have greater soil organic carbon, helping to increase the water holding capacity (43). Our results also showed that the  $\theta_{\text{crit}}$  and  $S$  have opposite responses to all these environmental factors (soil texture,  $\text{LAI}_{\text{max}}$ , VPD, and precipitation; Fig. 3, B to E and G to J). We noted that these environmental factors only explained about 40% of the variance in  $\theta_{\text{crit}}$ ,  $S$ , and  $\text{EF}_{\text{max}}$ . The portion of unexplained variance might be

related to plant hydraulic or functional traits, such as rooting depth or ability of roots to switch from surface to deep water uptake (44–47) and hydraulic traits diversity (48). Diverse communities are more likely to contain species with different traits that regulate how they respond to drought; higher hydraulic diversity, for example, buffers variation in ecosystem fluxes during dry periods across temperate and boreal forests (48). Given the large variations of these parameters over diverse ecosystems and the limited observational data that we could use, we provide here a comprehensive analysis across global sites.

Our study sheds a new light on varying EF-SM relationships in different ecosystems. Dryland ecosystems, such as savannas, operate at low  $\theta_{\text{crit}}$ . Across sites, there is a negative relationship between  $\theta_{\text{crit}}$  and  $S$ , indicating that dryland ecosystems, which minimize  $\theta_{\text{crit}}$  through mechanisms of sustained soil water extraction and plant hydraulic transport, are also more vulnerable once extreme stress below  $\theta_{\text{crit}}$  is reached. There is therefore a trade-off between  $\theta_{\text{crit}}$  and  $S$ : Sites with low  $\theta_{\text{crit}}$  values often have high  $S$  values, while sites with high  $\theta_{\text{crit}}$  values often have low  $S$  values, indicating two different adaptation strategies. The first strategy reflects a resistance to soil dryness and is more successful for ecosystems experiencing frequent dry-downs. However, below the infrequently reached  $\theta_{\text{crit}}$  value, ecosystem function may collapse rapidly. The second strategy with a high  $\theta_{\text{crit}}$  is more adapted to humid and subhumid environments where dry-downs are shorter and less severe. For the first strategy, the higher  $S$  values correspond to a more rapid stomatal closure in response to an SM decrease under water-limited conditions to prevent hydraulic failure (49, 50). In contrast, for the second strategy, the lower  $S$  values which are related to a more gradual stomatal closure in response to an SM decrease, benefit photosynthesis in periods of limited water stress, and reduce the risk of carbon starvation, but this can lead to hydraulic failure if drought is sufficiently intense: Plants will run out of water before they run out of carbon (51).

The  $\theta_{\text{crit}}$  values quantified in this study reflect a background ecosystem resistance to aridity. Berdugo *et al.* (52) recently reported that aridification is associated to systemic and abrupt changes, which occurred sequentially in three phases characterized by abrupt decays in plant productivity, soil fertility, and plant cover and richness at aridity values of 0.54, 0.7, and 0.8, respectively. Our results imply that ecosystems with lower  $\theta_{\text{crit}}$  should have higher aridity thresholds. We do not have a map of  $\theta_{\text{crit}}$ , but with advances in remote sensing, this may be possible [e.g., Feldman *et al.* (18)], and we could then test whether systems with a higher  $\theta_{\text{crit}}$  have a lower threshold response to increased aridity compared to more resistant systems with a lower  $\theta_{\text{crit}}$ . Consistent with the ecosystem optimality concepts, our results showed that the trade-off between  $\theta_{\text{crit}}$  and  $S$  helps to increase the growing-season EF and that optimal adaptation of the EF-SM response also maximizes growing-season carbon uptake. Note that different rooting depths across different sites may affect the  $\theta_{\text{crit}}$ , although recent studies showed that surface and rootzone SM are equivalently skillful for identifying evapotranspiration regime changes (36). We also noted that some species could use adaptation strategies to reduce LAI (e.g., drought deciduous functional types) in addition to stomatal regulation during dry periods (53, 54), but our analysis focused on peak growing season and soil dry-downs at short time scales; thus, the impacts of drought deciduousness should be muted. Moreover, our analysis of the temporal dynamics of  $\theta_{\text{crit}}$  showed that the interannual variability of  $\theta_{\text{crit}}$  is not significant (fig. S6), indicating the relative stability of  $\theta_{\text{crit}}$  through time in this study.

In summary, this study quantified the  $\theta_{\text{crit}}$ ,  $S$ , and  $EF_{\text{max}}$  in terrestrial ecosystems using globally distributed eddy covariance measurement sites. Our formulation is similar to one commonly used in land surface models, although models consider deeper SM than observations. We found systematic differences of the three parameters across biomes and climates and uncovered the relationships between parameter values and environmental factors, including climatic, biotic, and edaphic variables. These results help in identifying tipping points of water stress impairing ecosystem functioning and should help toward a better representation of water stress in land surface models. Future research will aim to use our new understanding of  $\theta_{\text{crit}}$ ,  $S$ , and  $EF_{\text{max}}$  to improve model representation of SM constraints on water and carbon fluxes. As soil matric potential and VPD interact with vegetation function to control water flow, future research deriving relationships between SM during dry-downs, VPD, and soil water potentials will be a central challenge.

## MATERIALS AND METHODS

### Eddy covariance observations

We used half-hourly SM, latent heat flux, sensible heat flux, VPD, GPP, and precipitation from the recently released ICOS (Integrated Carbon Observation System) (55), AmeriFlux (56, 57), and the FLUXNET2015 dataset of energy, water, and carbon fluxes and meteorological data, all of which have undergone a standardized set of quality control and gap filling (58, 59). Data were processed following a consistent and uniform processing pipeline (58). There are 279 flux tower sites in total by combing ICOS, AmeriFlux, and FLUXNET2015 datasets. We first removed 62 sites without SM measurements and then dropped all wetland sites because they have a perched water table and infrequently show SM limitations such that 212 sites remained. Because, for some sites, there was no dry-down detected during the peak growing season across all available years, these sites were also excluded (195 sites remaining). The EF-SM relationships in these 195 sites were evaluated to detect the  $\theta_{\text{crit}}$  for each site.

SM was measured as volumetric soil water content (percentage) at different depths. Surface SM (SM\_1: 0 to 10 cm, varying across sites) was measured at all sites, and some sites also provided deeper SM measurements (e.g., SM\_2: 10 to 30 cm; SM\_3: 20 to 60 cm). We mainly explored the surface SM observations, but deeper SM measurements were also used when available. The GPP estimates from the nighttime partitioning method were used for the analysis (60). Data were quality controlled so that only measured and good-quality gap-filled data (quality control = 0 or 1) were used. Daytime half-hourly data (9 a.m. to 16 p.m. local standard time) were averaged to daily values, while SM values were averaged over the full day.

### SM dry-down identification

Dry-downs following rainfall are episodes with no rain for several consecutive days during which SM shows a short-term “pulse” rise after rain and then decays until the next rain event. A dry-down is retained for our analysis when SM decreases consecutively for at least 10 days after rainfall following previous studies (13, 26, 27, 61, 62). Days with intermittent rainfall are excluded to remove the rainfall impacts on latent heat flux measurements. To minimize the irrigation effects on EF in croplands, we checked whether there were peaks of SM without rain at each cropland site, which would indicate irrigation events. Then, we removed the dry-downs with intense irrigation

episodes at cropland sites. We focused on the soil dry-downs during the peak growing season for all available site years, defined as 3-month period with the maximum mean GPP across the available years. This resulted in 2035 dry-down events that form the basis of our study.

### $\theta_{\text{crit}}$ , $S$ , and $EF_{\text{max}}$ estimation using EF-SM method

We calculated the daily EF as the ratio of the observed latent heat flux to the sum of latent and sensible heat fluxes. Then, we characterized the EF-SM relationship at each site using all available soil dry-downs, from a regression between these two variables with a linear-plus-plateau model

$$EF = \begin{cases} EF_{\text{max}} + S(SM - \theta_{\text{crit}}) & \text{if } SM < \theta_{\text{crit}} \\ EF_{\text{max}} & \text{if } SM \geq \theta_{\text{crit}} \end{cases} \quad (1)$$

where  $EF_{\text{max}}$  is the maximum value of EF in absence of SM stress (energy-limited stage),  $S$  represents the slope of the linear increase phase (water-limited stage), and  $\theta_{\text{crit}}$  is the critical SM threshold. These three parameters and their SEs were simultaneously estimated by least-squares fit with the R software package “segmented” (63) for each site, leading to site-specific estimated values of  $EF_{\text{max}}$ ,  $S$ , and  $\theta_{\text{crit}}$ .  $\theta_{\text{crit}}$  is the break point until which EF increases linearly as a function of SM. The  $S$  represents the EF sensitivity to SM in the water-limited regime, indicating the magnitude of EF increase for each additional 1% soil water content (or  $0.01 \text{ m}^3 \text{ m}^{-3}$ ) change in SM when SM is below its break point. The plateau is the maximum EF value reached when SM exceeds its threshold. An example to estimate the  $EF_{\text{max}}$ ,  $S$ , and  $\theta_{\text{crit}}$  is shown in Fig. 1B.

On the basis of the EF-SM relationships, there were 85, 29, and 19 sites with the  $\theta_{\text{crit}}$  estimates using the first (SM\_1), second (SM\_2), and third (SM\_3) soil water content measurement depth, respectively. For the rest of the sites, it was not possible to estimate a  $\theta_{\text{crit}}$  because samples were too infrequent, or there were no thresholds. These 85 sites included 11 DBFs, 5 evergreen broadleaf forests, 26 evergreen needleleaf forests, 3 mixed forests, 8 shrublands, 4 croplands, 14 grasslands, and 14 savannas (table S1).

Differences in  $\theta_{\text{crit}}$ ,  $S$ , and  $EF_{\text{max}}$  between groups (different plant functional types or climate types) were analyzed using the Kruskal-Wallis test, a nonparametric test of difference (64). A  $P < 0.05$  was used to identify significant differences between groups. Plant functional types were defined according to the International Geosphere–Biosphere Programme classification (58). Climate types were defined according to the Köppen–Geiger classification as in Migliavacca *et al.* (65): tropical (Aw, Af, and Am), dry (BSh, BSk, and BWh), subtropical (Cfa, Csa, Csb, and Cwa), temperate (Cfb), continental (Dfa, Dfb, Dwa, Dwb, and Dwc), and boreal (Dfc and Dsc).

### $\theta_{\text{crit}}$ estimation using VPD-GPP-SM method

For the threshold in plant photosynthetic processes, Fu *et al.* (13) recently reported that the initiation of water stress could be detected as the SM value when the sign of the covariance between daily GPP and VPD changes from positive to negative during a dry-down. GPP and evapotranspiration are tightly coupled on short time scales (4), and the sign of the covariance between daily VPD and GPP reflects the relative strength of water versus energy limitation on ecosystem function, because VPD combines the effects of both water stress and energy demand (via temperature) on GPP (14–16). Following Fu *et al.* (13), we also calculated the covariance between daily VPD and GPP across 9-day moving windows during the dry-down (e.g.,

1 to 9 days, 2 to 10 days, and 3 to 11 days). A positive covariance indicates that higher VPD is associated with increases in GPP (which we term “radiation effects”), while a negative covariance indicates that water stress limits GPP, i.e., with a higher VPD caused by dryer soils results in a lower GPP. We excluded some short dry-downs because their covariances during the dry-down are all positive or negative, suggesting that the entire dry-down period is under energy-limited or water-limited stage. We only chose the long soil dry-downs with at least 15 days (with at least seven covariance values), and their covariances must include both positive and negative values. Similar to the VPD-GPP covariance, the average of SM during the moving window (e.g., 1 to 9 days, 2 to 10 days, and 3 to 11 days) was also calculated to detect the  $\theta_{\text{crit}}$  when the sign of VPD-GPP covariance changes from positive to negative. An example to quantify the  $\theta_{\text{crit}}$  using VPD-GPP-SM method is shown in Fig. 1C.

To compare the  $\theta_{\text{crit}}$  values from the VPD-GPP-SM method with that from the EF-SM method, we fitted the  $\theta_{\text{crit}}$  values from these two methods using linear [ $f(x) = p1 \times x + p2$ ] and nonlinear [ $f(x) = p1 \times x^2 + p2 \times x + p3$ ] function, respectively (fig. S1). We found that the coefficients of  $p1$  and  $p2$  in the linear fitting are significantly different from 0 at the significance level of 0.05, while both the  $p1$  and  $p3$  in the nonlinear fitting do not significantly differ from 0 (fig. S1), suggesting that the linear assumption is reasonable. To test whether the closure of the energy balance from eddy covariance measurements affects the bias of  $\theta_{\text{crit}}$  values (66), we repeated the analysis using the “LE.CORR” and “H.CORR” variables from FLUXNET database to calculate the EF and quantify  $\theta_{\text{crit}}$ , instead of “LE” and “H.” LE.CORR and H.CORR are the “energy balance–corrected” version of latent and sensible heat flux, based on the assumption that the Bowen ratio is correct (67). Our results were robust to either variable (fig. S2). The differences in SM threshold values based on the two energy fluxes were negligible (fig. S2).

### Drivers of the spatial variability of $\theta_{\text{crit}}$ , $S$ , and $EF_{\text{max}}$

A random forests analysis was used to identify the soil property, vegetation structure, and climate variables that contribute the most to the spatial variability of  $\theta_{\text{crit}}$ ,  $S$ , and  $EF_{\text{max}}$ . For climatic variables, we calculated the AI, mean VPD, incoming shortwave radiation, wind speed, and total precipitation during the peak growing season from flux tower observations at each site. As vegetation structure variable,  $LAI_{\text{max}}$  was collected for 53 sites, from the literature (65, 68, 69). Using the Application for Extracting and Exploring Analysis Ready Samples (AppEARS) (70),  $LAI_{\text{max}}$  values in the rest of 32 sites were extracted from MODIS LAI product (MCD15A2) at 500-m spatial resolution (71). Soil property variables were extracted from SoilGrids, a collections of soil property maps for the world at 250-m resolution (72), including sand fraction, soil organic carbon content, total nitrogen, pH, bulk density, volumetric fraction of coarse fragments, and cation exchange capacity.

The performances of random forests model were assessed by fivefold cross-validation using two criteria: the mean absolute error (MAE) and the  $R$ -squared value ( $R^2$ ). MAE quantifies the overall error, while  $R^2$  estimates the proportion of variance in response variable that is captured by the predictive variables. We favored the model with the smallest MAE and the highest  $R^2$  (73, 74). Following Huang *et al.* (73), we first run the random forests model with all predictor variables included and then sequentially excluded predictors that did not improve model performance one after another. The best model with the minimum number of predictors and same



predictors for all three response variables ( $\theta_{crit}$ , S, and  $EF_{max}$ ) was selected. The final set of predictors included the following predictor variables: as soil property variable, sand fraction (%); as vegetation structure variable,  $LAI_{max}$  (in square meters per square meter); as climatic variables, mean daily VPD (in hectopascals) and total precipitation amount (in millimeters) during the peak growing season.

We used partial dependencies of variables to assess the relationship between individual predictors and the response variables (that is,  $\theta_{crit}$ , S, or  $EF_{max}$ ). The results from the partial dependency analysis can be used to determine the effects of individual variables on the response, without the influence of the other variables (74). The partial dependencies were calculated restricted to the values falling within the convex hull of their training values to reduce the risk of interpreting the partial dependence plot outside the range of the data (extrapolation risk) (65). The partial dependence function was computed using the pdp R package (75). Partial dependence plots derived for  $\theta_{crit}$ , S, and  $EF_{max}$  are shown in Fig. 3 (B to E, G to J, and L to O) for various inputs.

**Temporal variability of  $\theta_{crit}$ , S, and  $EF_{max}$**

Besides their spatial variability across sites,  $\theta_{crit}$ , S, and  $EF_{max}$  may also change with time. Although the temporal variability in  $\theta_{crit}$ , S, and  $EF_{max}$  is difficult to evaluate given the relatively short observation record at most sites, we analyzed the temporal dynamics of these three parameters at a forest site with long observational periods (2000–2019), DE-Hai (table S1). We quantified  $\theta_{crit}$ , S, and  $EF_{max}$  using dry-downs every 3 years, respectively (table S2; note that we could not estimate a  $\theta_{crit}$  during 2009–2017 because samples were too infrequent, or SM was always above or below the threshold in these years). We found that  $\theta_{crit}$  values changed slightly over time (table S2). The mean  $\theta_{crit}$ , S, and  $EF_{max}$  across results from every 3 years were similar to that of during 2000–2019; thus, our results reflect the average of  $\theta_{crit}$ , S, and  $EF_{max}$  during the available observational periods. To further test whether there was a trend change through time in  $\theta_{crit}$ , S, and  $EF_{max}$ , we performed the same analysis at five sites with at least 15 years of measurements. We found that there was no significant trend change with time in the three parameters over all site years (fig. S6). This initial exploration should be treated with caution given the relatively few sites and short observation record.

**Relationships between  $\theta_{crit}$ , S, and  $EF_{max}$**

To understand the relationships between  $\theta_{crit}$ , S, and  $EF_{max}$ , we plotted these three variables in three dimensions across all sites, distributed in different biomes or AI. AI was defined as the ratio of annual PET to annual precipitation. We calculated the PET using the Priestley-Taylor equation following Novick *et al.* (16) for each site. The AI calculated using PET from Priestley-Taylor equation matched well with that of the Penman-Monteith equation. We also performed the partial correlation analysis to test the significance of the relationships between  $\theta_{crit}$ , S, and  $EF_{max}$  ( $P < 0.05$ ).

To further explore the negative relationship between  $\theta_{crit}$  and S, we define the intersection of the fitted segmented curve with the x axis as  $\theta_0$  (the value of SM at which EF is equal to zero); thus,  $\theta_0$  can be calculated using the Eq. 2

$$S = \frac{EF_{max}}{(\theta_{crit} - \theta_0)} \tag{2}$$

We then compared the  $\theta_0$  with zero using *t* test across sites and found that the  $\theta_0$  does not significantly differ from zero (fig. S7). The S values in different biomes can therefore be predicted using the ratio of  $EF_{max}$  and  $\theta_{crit}$  (fig. S8).

**Mean response function of EF-SM in savannas and grasslands**

On the basis of the distribution of  $\theta_{crit}$  and S in different plant functional types, we proposed two schema: (i) low  $\theta_{crit}$  with high S (e.g., savannas) and (ii) high  $\theta_{crit}$  with low S (e.g., grasslands). As both  $\theta_{crit}$  and S were significantly different between savannas and grasslands (Fig. 2, A and C) and the number of sites in savannas ( $n = 14$ ) and grasslands ( $n = 14$ ) were same, the response functions of EF-SM in these two biomes were further compared. We were not able to compare the response functions of EF-SM among other biomes because they did not show any significant difference in either  $\theta_{crit}$  or S (Fig. 2, A and C). The mean response functions of EF-SM in savannas and grasslands were obtained by calculating the median values of the  $\theta_{crit}$ , S, and  $EF_{max}$  across all sites for savannas and grasslands, respectively. The uncertainty of mean EF-SM response function for each biome was quantified by calculating the 95% confidence interval across all sites.

**Derivation of  $G_c$  from eddy covariance measurements**

At each site in savannas and grasslands,  $G_c$  under water-limited stage ( $SM < \theta_{crit}$ ) was calculated using half-hourly eddy covariance measurements by inverting the Penman-Monteith equation (76)

$$G_c = r_a \gamma / \left( \frac{\Delta(R_n - G) + \rho c_p r_a (e_s(T_a) - e_a)}{\lambda E} - (\Delta + \lambda) \right) \tag{3}$$

where  $G_c$  and  $r_a$  are canopy stomatal conductance and aerodynamic resistance, respectively;  $\gamma$  is the psychrometric constant;  $\Delta$  is the S of the water vapor deficit with respect to temperature;  $R_n$  and  $G$  are observed net radiation and soil heat flux, respectively;  $\rho$  is air density,  $C_p$  is the specific heat capacity of dry air;  $e_s$  and  $e_a$  are saturated and actual vapor pressure, respectively; and  $\lambda E$  is observed evapotranspiration.  $r_a$  is calculated following Novick *et al.* (16) (Eq. 4), using the von Kármán constant ( $k = 0.4$ ), available wind speed data ( $w_s$ ), measurement height ( $z_m$ ), momentum roughness length ( $z_0 = 0.1h$ ), and zero plane displacement ( $z_d = 0.67h$ ), both based on calculated canopy height ( $h$ ) under near-neutral conditions (Eq. 5) (77)

$$r_a = \frac{\ln\left(\frac{z_m - z_d}{z_0}\right)^2}{w_s k^2} \tag{4}$$

$$h = \frac{z_m}{0.6 + 0.1 \times \exp\left(\frac{k w_s}{u^*}\right)} \tag{5}$$

To evaluate the reduction rate of  $G_c$  per SM decrease under water-limited stage, we further calculated the change rate of  $G_c$  under water-limited stage for each site in savannas and grasslands by the ratio between the change of  $G_c$  and the change of SM as follows (Eq. 6)

$$\Delta G_c = \frac{\text{Median}(G_{SM \text{ in } 80-100\text{th}}) - \text{Median}(G_{SM \text{ in } 0-20\text{th}})}{\text{Median}(SM_{80-100\text{th}}) - \text{Median}(SM_{0-20\text{th}})} \tag{6}$$

where  $\Delta G_c$  is the reduction rate of  $G_c$  per SM decrease,  $\text{Median}(G_{SM \text{ in } 80-100\text{th}})$  is the median  $G_c$  during the 80th to 100th percentiles of SM under

Downloaded from https://www.science.org at Max Planck Society on February 23, 2023

water-limited stage, Median( $G_{SM}$  in 0–20th) is the median  $G_c$  during the 0th to 20th percentiles of SM under water-limited stage, Median( $SM_{80-100th}$ ) is the median SM during the 80th to 100th percentiles of SM under water-limited stage, and Median( $SM_{0-20th}$ ) is the median SM during the 0th to 20th percentiles of SM under water-limited stage.

### Predicting EF and GPP during the peak growing season

We formulated the hypothesis that the distinct response functions of EF-SM between savannas (low  $\theta_{crit}$  with high S) and grasslands (high  $\theta_{crit}$  with low S) locally maximize growing-season EF. To test this, we predicted the mean daily EF during the peak growing season in savannas by swapping two response functions of EF-SM: one from savannas and one from grasslands. Similarly, we predicted mean daily EF during the peak growing season in grasslands for each site using daily SM in grasslands and running two response functions of EF-SM, respectively.

To further test whether the maximizing EF also reflect a production maximization during the peak growing season, we performed the same analysis for savannas and grasslands GPP using daily observed EF and predicted EF from two response functions of EF-SM, respectively. Mean daily GPP during the peak growing season for each site was calculated using daily EF, net radiation ( $R_n$ ), and water use efficiency (WUE) as Eq. 7. WUE was calculated as the ratio of the observed GPP to the observed latent heat flux (78). Except for savannas and grasslands, we cannot compare the response functions of EF-SM among other biomes because they have no significant difference in either  $\theta_{crit}$  or S (Fig. 2, A and C)

$$GPP = EF \times R_n \times WUE \quad (7)$$

### SUPPLEMENTARY MATERIALS

Supplementary material for this article is available at <https://science.org/doi/10.1126/sciadv.abq7827>

### REFERENCES AND NOTES

- M. Bassiouni, S. P. Good, C. J. Still, C. W. Higgins, Plant water uptake thresholds inferred from satellite soil moisture. *Geophys. Res. Lett.* **47**, e2020GL087077 (2020).
- I. Rodríguez-Iturbe, Ecohydrology: A hydrologic perspective of climate-soil-vegetation dynamics. *Water Resour. Res.* **36**, 3–9 (2000).
- P. Gentine, A. Chhang, A. Rigden, G. Salvucci, Evaporation estimates using weather station data and boundary layer theory. *Geophys. Res. Lett.* **43**, 11,661–11,670 (2016).
- P. Gentine, J. K. Green, M. Guérin, V. Humphrey, S. I. Seneviratne, Y. Zhang, S. Zhou, Coupling between the terrestrial carbon and water cycles—A review. *Environ. Res. Lett.* **14**, 083003 (2019).
- S. I. Seneviratne, T. Corti, E. L. Davin, M. Hirschi, E. B. Jaeger, I. Lehner, B. Orlowsky, A. J. Teuling, Investigating soil moisture–climate interactions in a changing climate: A review. *Earth Sci. Rev.* **99**, 125–161 (2010).
- C. Schwingshackl, M. Hirschi, S. I. Seneviratne, Quantifying spatiotemporal variations of soil moisture control on surface energy balance and near-surface air temperature. *J. Climate* **30**, 7105–7124 (2017).
- I. Rodríguez-Iturbe, A. Porporato, *Ecohydrology of Water-Controlled Ecosystems: Soil Moisture and Plant Dynamics* (Cambridge Univ. Press, 2007).
- F. Laio, A. Porporato, L. Ridolfi, I. Rodríguez-Iturbe, Plants in water-controlled ecosystems: Active role in hydrologic processes and response to water stress: II. Probabilistic soil moisture dynamics. *Adv. Water Resour.* **24**, 707–723 (2001).
- J. A. Santanello Jr., P. A. Dirmeyer, C. R. Ferguson, K. L. Findell, A. B. Tawfik, A. Berg, M. Ek, P. Gentine, B. P. Guillod, C. Van Heerwaarden, Land–atmosphere interactions: The LoCo perspective. *Bull. Am. Meteorol. Soc.* **99**, 1253–1272 (2018).
- P. Zhang, J.-H. Jeong, J.-H. Yoon, H. Kim, S.-Y. S. Wang, H. W. Linderholm, K. Fang, X. Wu, D. Chen, Abrupt shift to hotter and drier climate over inner East Asia beyond the tipping point. *Science* **370**, 1095–1099 (2020).
- M. I. Budyko, *Climate and Life* (Academic Press, 1974).
- P. S. Eagleson, Climate, soil, and vegetation: 4. The expected value of annual evapotranspiration. *Water Resour. Res.* **14**, 731–739 (1978).
- Z. Fu, P. Ciais, D. Makowski, A. Bastos, P. C. Stoy, A. Ibrom, A. Knohl, M. Migliavacca, M. Cuntz, L. Sigut, M. Peichl, D. Loustau, T. S. El-Madany, N. Buchmann, M. Gharun, I. Janssens, C. Markwitz, T. Grunwald, C. Rebmann, M. Molder, A. Varlagin, I. Mammarella, P. Kolari, C. Bernhofer, M. Heliasz, C. Vincke, A. Pitacco, E. Cremonese, L. Foltynova, J. P. Wigneron, Uncovering the critical soil moisture thresholds of plant water stress for European ecosystems. *Glob. Chang. Biol.* **28**, 2111–2123 (2021).
- C. Gossiorid, T. N. Buckley, L. A. Cernusak, K. A. Novick, B. Poulter, R. T. Siegwolf, J. S. Sperry, N. G. McDowell, Plant responses to rising vapor pressure deficit. *New Phytol.* **226**, 1550–1566 (2020).
- H. Kimm, K. Guan, P. Gentine, J. Wu, C. J. Bernacchi, B. N. Sulman, T. J. Griffis, C. Lin, Redefining droughts for the U.S. Corn Belt: The dominant role of atmospheric vapor pressure deficit over soil moisture in regulating stomatal behavior of Maize and Soybean. *Agric. For. Meteorol.* **287**, 107930 (2020).
- K. A. Novick, D. L. Ficklin, P. C. Stoy, C. A. Williams, G. Bohrer, A. C. Oishi, S. A. Papuga, P. D. Blanken, A. Noormets, B. N. Sulman, R. L. Scott, L. Wang, R. P. Phillips, The increasing importance of atmospheric demand for ecosystem water and carbon fluxes. *Nat. Clim. Change* **6**, 1023–1027 (2016).
- A. G. Pendergrass, G. A. Meehl, R. Pulwarty, M. Hobbins, A. Hoell, A. AghaKouchak, C. J. Bonfils, A. J. Gallant, M. Hoerling, D. Hoffmann, L. Kaatz, F. Lehner, D. Llewellyn, P. Mote, R. B. Neale, J. T. Overpeck, A. Sheffield, K. Stahl, M. Svoboda, M. C. Wheeler, A. W. Wood, C. A. Woodhouse, Flash droughts present a new challenge for subseasonal-to-seasonal prediction. *Nat. Clim. Change* **10**, 191–199 (2020).
- A. F. Feldman, D. J. Short Gianotti, I. F. Trigo, G. D. Salvucci, D. Entekhabi, Satellite-based assessment of land surface energy partitioning–soil moisture relationships and effects of confounding variables. *Water Resour. Res.* **55**, 10657–10677 (2019).
- A. Porporato, P. D'odorico, F. Laio, L. Ridolfi, I. Rodríguez-Iturbe, Ecohydrology of water-controlled ecosystems. *Adv. Water Resour.* **25**, 1335–1348 (2002).
- S. I. Seneviratne, M. Wilhelm, T. Stanelle, B. van den Hurk, S. Hagemann, A. Berg, F. Cheruy, M. E. Higgins, A. Meier, V. Brovkin, M. Claussen, A. Ducharme, J.-L. Dufresne, K. L. Findell, J. Ghattas, D. M. Lawrence, S. Malyshev, M. Rummukainen, B. Smith, Impact of soil moisture–climate feedbacks on CMIP5 projections: First results from the GLACE-CMIP5 experiment. *Geophys. Res. Lett.* **40**, 5212–5217 (2013).
- A. K. Betts, Understanding hydrometeorology using global models. *Bull. Am. Meteorol. Soc.* **85**, 1673–1688 (2004).
- D. D. Baldocchi, L. Xu, N. Kiang, How plant functional-type, weather, seasonal drought, and soil physical properties alter water and energy fluxes of an oak–grass savanna and an annual grassland. *Agric. For. Meteorol.* **123**, 13–39 (2004).
- R. Koster, S. Schubert, M. Suarez, Analyzing the concurrence of meteorological droughts and warm periods, with implications for the determination of evaporative regime. *J. Climate* **22**, 3331–3341 (2009).
- K. W. Oleson, D. M. Lawrence, B. Gordon, M. G. Flanner, E. Kluzek, J. Peter, S. Levis, S. C. Swenson, E. Thornton, J. Feddema, “Technical description of version 4.0 of the Community Land Model (CLM)” (Technical Note No. NCAR/TN-478+STR, University Corporation for Atmospheric Research, 2010).
- P. A. Dirmeyer, R. D. Koster, Z. Guo, Do global models properly represent the feedback between land and atmosphere? *J. Hydrometeorol.* **7**, 1177–1198 (2006).
- R. Akbar, D. J. S. Gianotti, K. A. McColl, E. Haghighi, G. D. Salvucci, D. Entekhabi, Estimation of landscape soil water losses from satellite observations of soil moisture. *J. Hydrometeorol.* **19**, 871–889 (2018).
- A. F. Feldman, D. J. S. Gianotti, A. G. Konings, K. A. McColl, R. Akbar, G. D. Salvucci, D. Entekhabi, Moisture pulse-reserve in the soil-plant continuum observed across biomes. *Nat. Plants* **4**, 1026–1033 (2018).
- T. F. Keenan, M. Migliavacca, D. Papale, D. Baldocchi, M. Reichstein, M. Torn, T. Wutzler, Widespread inhibition of daytime ecosystem respiration. *Nat. Ecol. Evol.* **3**, 407–415 (2019).
- A. Gerrits, H. Savenije, E. Veling, L. Pfister, Analytical derivation of the Budyko curve based on rainfall characteristics and a simple evaporation model. *Water Resour. Res.* **45**, W04403 (2009).
- G. Bonan, *Climate Change and Terrestrial Ecosystem Modeling* (Cambridge Univ. Press, 2019).
- K. Van Looy, J. Bouma, M. Herbst, J. Koestel, B. Minasny, U. Mishra, C. Montzka, A. Nemes, Y. A. Pachepsky, J. Padarian, M. G. Schaap, B. Tóth, A. Verhoef, J. Vanderborght, M. J. van der Ploeg, L. Weiermüller, S. Zacharias, Y. Zhang, H. Vereecken, Pedotransfer functions in Earth system science: Challenges and perspectives. *Rev. Geophys.* **55**, 1199–1256 (2017).
- W. Kolby Smith, S. C. Reed, C. C. Cleveland, A. P. Ballantyne, W. R. Anderegg, W. R. Wieder, Y. Y. Liu, S. W. Running, Large divergence of satellite and Earth system model estimates of global terrestrial CO<sub>2</sub> fertilization. *Nat. Clim. Change* **6**, 306–310 (2016).
- Y. Pei, J. Dong, Y. Zhang, W. Yuan, R. Doughty, J. Yang, D. Zhou, L. Zhang, X. Xiao, Evolution of light use efficiency models: Improvement, uncertainties, and implications. *Agric. For. Meteorol.* **317**, 108905 (2022).

34. B. D. Stocker, J. Zscheischler, T. F. Keenan, I. C. Prentice, S. I. Seneviratne, J. Peñuelas, Drought impacts on terrestrial primary production underestimated by satellite monitoring. *Nat. Geosci.* **12**, 264–270 (2019).
35. J. Buitink, A. M. Swank, M. van der Ploeg, N. E. Smith, H.-J. F. Benninga, F. van der Bolt, C. D. Carranza, G. Koren, R. van der Velde, A. J. Teuling, Anatomy of the 2018 agricultural drought in the Netherlands using in situ soil moisture and satellite vegetation indices. *Hydrol. Earth Syst. Sci.* **24**, 6021–6031 (2020).
36. J. Dong, R. Akbar, D. J. Short Gianotti, A. F. Feldman, W. T. Crow, D. Entekhabi, Can surface soil moisture information identify evapotranspiration regime transitions? *Geophys. Res. Lett.* **49**, e2021GL097697 (2022).
37. G. Bonan, *Ecological Climatology: Concepts and Applications* (Cambridge Univ. Press, 2015).
38. Y. Shao, P. Irannejad, On the choice of soil hydraulic models in land-surface schemes. *Bound.-Lay. Meteorol.* **90**, 83–115 (1999).
39. K. A. Novick, D. L. Ficklin, D. Baldocchi, K. J. Davis, T. A. Ghezzehei, A. G. Konings, N. MacBean, N. Raouf, R. L. Scott, Y. Shi, B. N. Sulman, J. D. Wood, Confronting the water potential information gap. *Nat. Geosci.* **15**, 158–164 (2022).
40. M. T. Van Genuchten, A closed-form equation for predicting the hydraulic conductivity of unsaturated soils. *Soil Sci. Soc. Am. J.* **44**, 892–898 (1980).
41. Y. Mualem, A new model for predicting the hydraulic conductivity of unsaturated porous media. *Water Resour. Res.* **12**, 513–522 (1976).
42. I. N. Williams, M. S. Torn, Vegetation controls on surface heat flux partitioning, and land-atmosphere coupling. *Geophys. Res. Lett.* **42**, 9416–9424 (2015).
43. W. Chen, P. Ciais, D. Zhu, A. Ducharne, N. Viovy, C. Qiu, C. Huang, Feedbacks of soil properties on vegetation during the Green Sahara period. *Quat. Sci. Rev.* **240**, 106389 (2020).
44. Y. Liu, N. M. Holtzman, A. G. Konings, Global ecosystem-scale plant hydraulic traits retrieved using model–data fusion. *Hydrol. Earth Syst. Sci.* **25**, 2399–2417 (2021).
45. J. Kattge, S. Diaz, S. Lavorel, I. C. Prentice, P. Leadley, G. Bönisch, E. Garnier, M. Westoby, P. B. Reich, I. J. Wright, TRY – A global database of plant traits. *Glob. Chang. Biol.* **17**, 2905–2935 (2011).
46. Y. Fan, G. Miguez-Macho, E. G. Jobbágy, R. B. Jackson, C. Otero-Casal, Hydrologic regulation of plant rooting depth. *Proc. Natl. Acad. Sci.* **114**, 10572–10577 (2017).
47. Y. Yang, R. J. Donohue, T. R. McVicar, Global estimation of effective plant rooting depth: Implications for hydrological modeling. *Water Resour. Res.* **52**, 8260–8276 (2016).
48. W. R. Anderegg, A. G. Konings, A. T. Trugman, K. Yu, D. R. Bowling, R. Gabbitas, D. S. Karp, S. Pacala, J. S. Sperry, B. N. Sulman, Hydraulic diversity of forests regulates ecosystem resilience during drought. *Nature* **561**, 538–541 (2018).
49. A. G. Konings, P. Gentine, Global variations in ecosystem-scale isohydricity. *Glob. Chang. Biol.* **23**, 891–905 (2017).
50. N. G. McDowell, Mechanisms linking drought, hydraulics, carbon metabolism, and vegetation mortality. *Plant Physiol.* **155**, 1051–1059 (2011).
51. N. McDowell, W. T. Pockman, C. D. Allen, D. D. Breshears, N. Cobb, T. Kolb, J. Plaut, J. Sperry, A. West, D. G. Williams, E. A. Yezpe, Mechanisms of plant survival and mortality during drought: Why do some plants survive while others succumb to drought? *New Phytol.* **178**, 719–739 (2008).
52. M. Berdugo, M. Delgado-Baquerizo, S. Soliveres, R. Hernández-Clemente, Y. Zhao, J. J. Gaitán, N. Gross, H. Saiz, V. Maire, A. Lehmann, M. C. Rillig, R. V. Sole, F. T. Maestre, Global ecosystem thresholds driven by aridity. *Science* **367**, 787–790 (2020).
53. W. K. Smith, M. P. Dannenberg, D. Yan, S. Herrmann, M. L. Barnes, G. A. Barron-Gafford, J. A. Biederman, S. Ferrenberg, A. M. Fox, A. Hudson, J. F. Knowles, N. MacBean, D. J. P. Moore, P. L. Nagler, S. C. Reed, W. A. Rutherford, R. L. Scott, X. Wang, J. Yang, Remote sensing of dryland ecosystem structure and function: Progress, challenges, and opportunities. *Remote Sens. Environ.* **233**, 111401 (2019).
54. K. Dahlin, R. Fisher, P. Lawrence, Environmental drivers of drought deciduous phenology in the Community Land Model. *Biogeosciences* **12**, 5061–5074 (2015).
55. Warm Winter 2020 Team, & ICOS Ecosystem Thematic Centre. (2022). Warm Winter 2020 ecosystem eddy covariance flux product for 73 stations in FLUXNET-Archive format—release 2022-1 (version 1.0). ICOS Carbon Portal; <https://doi.org/10.18160/2G60-ZHAK>.
56. K. A. Novick, J. Biederman, A. Desai, M. Litvak, D. J. Moore, R. Scott, M. Torn, The AmeriFlux network: A coalition of the willing. *Agric. For. Meteorol.* **249**, 444–456 (2018).
57. X. Lu, T. F. Keenan, No evidence for a negative effect of growing season photosynthesis on leaf senescence timing. *Glob. Chang. Biol.* **28**, 3083–3093 (2022).
58. G. Pastorello, C. Trotta, E. Canfora, H. Chu, D. Christianson, Y.-W. Cheah, C. Poindexter, J. Chen, A. Elbashandy, M. Humphrey, P. Isaac, D. Polidori, M. Reichstein, A. Ribeca, C. van Ingem, N. Vuichard, L. Zhang, B. Amiro, C. Ammann, M. A. Arain, J. Ardö, T. Arkebauer, S. K. Arndt, N. Arriga, M. Aubinet, M. Aurela, D. Baldocchi, A. Barr, E. Beamesderfer, L. B. Marchesini, O. Bergeron, J. Beringer, C. Bernhofer, D. Berveiller, D. Billesbach, T. A. Black, P. D. Blanken, G. Bohrer, J. Boike, P. V. Bolstad, D. Bonal, J.-M. Bonnefond, D. R. Bowling, R. Bracho, J. Brodeur, C. Brümmer, N. Buchmann, B. Burban, S. P. Burns, P. Buysse, P. Cale, M. Cavagna, P. Cellier, S. Chen, I. Chini, T. R. Christensen, J. Cleverly, A. Collalti, C. Consalvo, B. D. Cook, D. Cook, C. Coursolle, E. Cremonese, P. S. Curtis, E. D’Andrea, H. da Rocha, X. Dai, K. J. Davis, B. De Cinti, A. De Grandcourt, A. De Ligne, R. C. De Oliveira, N. Delpierre, A. R. Desai, C. M. Di Bella, P. di Tommasi, H. Dolman, F. Domingo, G. Dong, S. Dore, P. Duce, E. Dufrêne, A. Dunn, J. Dušek, D. Eamus, U. Eichelmann, H. A. M. El Khidir, W. Eugster, C. M. Ewenz, B. Ewers, D. Famulari, S. Fares, I. Feigenwinter, A. Feitz, R. Fensholt, G. Filippa, M. Fischer, J. Frank, M. Galvagno, M. Gharun, D. Gianelle, B. Gielen, B. Gioli, A. Gitelson, I. Godeb, M. Goeckede, A. H. Goldstein, C. M. Gough, M. L. Goulden, A. Graf, A. Griebel, C. Gruening, T. Grünwald, A. Hammerle, S. Han, X. Han, B. U. Hansen, C. Hanson, J. Hatakka, Y. He, M. Hehn, B. Heinesch, N. Hinko-Najera, L. Hörtnagl, L. Hutley, A. Ibrom, H. Ikawa, M. Jackowicz-Korczynski, D. Janouš, W. Jans, R. Jassal, S. Jiang, T. Kato, M. Khomik, J. Klatt, A. Knohl, S. Knox, H. Kobayashi, G. Koerber, O. Kolle, Y. Kosugi, A. Kotani, A. Kowalski, B. Kruijt, J. Kurbatova, W. L. Kutsch, H. Kwon, S. Launiainen, T. Laurila, B. Law, R. Leuning, Y. Li, M. Liddell, J.-M. Limousin, M. Lion, A. J. Liska, A. Lohila, A. López-Ballesteros, E. López-Blanco, B. Loubet, D. Loustau, A. Lucas-Moffat, J. Lüers, S. Ma, C. Macfarlane, V. Magliulo, R. Maier, I. Mammarella, G. Manca, B. Marcolla, H. A. Margolis, S. Marras, W. Massman, M. Mastepanov, R. Matamala, J. H. Matthes, F. Mazzenga, H. M. Caughey, I. M. Hugh, A. M. S. Mc Millan, L. Merbold, W. Meyer, T. Meyers, S. D. Miller, S. Minerbi, U. Møderow, R. K. Monson, L. Montagnani, C. E. Moore, E. Moors, V. Moreaux, C. Moureaux, J. W. Munger, T. Nakai, J. Neiryck, Z. Nescic, G. Nicolini, A. Noormets, M. Northwood, M. Nosoetto, Y. Nouvellon, K. Novick, W. Oechel, J. E. Olesen, J.-M. Ourcival, S. A. Papuga, F.-J. Parmentier, E. Paul-Limoges, M. Pavelka, M. Peichl, E. Pendall, R. P. Phillips, K. Pilegaard, N. Pirk, G. Posse, T. Powell, H. Prasse, S. M. Prober, S. Rambal, Ü. Rannik, N. Raz-Yaseef, C. Rebmann, D. Reed, V. R. de Dios, N. Restrepo-Coupe, B. R. Reverter, M. Roland, S. Sabbatini, T. Sachs, S. R. Saleska, E. P. Sánchez-Cañete, Z. M. Sanchez-Mejia, H. P. Schmid, M. Schmidt, K. Schneider, F. Schrader, I. Schroder, R. L. Scott, P. Sedláč, P. Serrano-Ortiz, C. Shoar, P. Shi, I. Shironya, L. Siebke, L. Šigut, R. Silberstein, C. Sirca, D. Spano, R. Steinbrecher, R. M. Stevens, C. Sturtevant, A. Stuyker, T. Tagesson, S. Takahashi, Y. Tang, N. Tapper, J. Thom, M. Tomassucci, J.-P. Tuovinen, S. Urbanski, R. Valentini, M. van der Molen, E. van Gorsel, K. van Huissteden, A. Varlagin, J. Verfaillie, T. Vesala, C. Vincke, D. Vitale, N. Vygodskaya, J. P. Walker, E. Walter-Shea, H. Wang, R. Weber, S. Westermann, C. Wille, S. Wofsy, G. Wohlfahrt, S. Wolf, W. Woodgate, Y. Li, R. Zampieri, J. Zhang, G. Zhou, D. Zona, D. Agarwal, S. Biraud, M. Torn, D. Papale, The FLUXNET2015 dataset and the ONEFlux processing pipeline for eddy covariance data. *Sci. Data* **7**, 225 (2020).
59. D. Baldocchi, E. Falge, L. Gu, R. Olson, D. Hollinger, S. Running, P. Anthoni, C. Bernhofer, K. Davis, R. Evans, J. Fuentes, A. Goldstein, G. Katul, B. Law, X. Lee, Y. Malhi, T. Meyers, W. Munger, W. Oechel, K. T. Paw U, K. Pilegaard, H. P. Schmid, R. Valentini, S. Verma, T. Vesala, K. Wilson, S. Wofsy, FLUXNET: A new tool to study the temporal and spatial variability of ecosystem-scale carbon dioxide, water vapor, and energy flux densities. *Bull. Am. Meteorol. Soc.* **82**, 2415–2434 (2001).
60. M. Reichstein, E. Falge, D. Baldocchi, D. Papale, M. Aubinet, P. Berbigier, C. Bernhofer, N. Buchmann, T. Gilmanov, A. Granier, T. Grünwald, K. Havránková, H. Ilvesniemi, D. Janous, A. Knohl, T. Laurila, A. Lohila, D. Loustau, G. Matteucci, T. Meyers, F. Miglietta, J.-M. Ourcival, J. Pumpanen, S. Rambal, E. Rotenberg, M. Sanz, J. Tenhunen, G. Seufert, F. Vaccari, T. Vesala, D. Yakir, R. Valentini, On the separation of net ecosystem exchange into assimilation and ecosystem respiration: Review and improved algorithm. *Glob. Chang. Biol.* **11**, 1424–1439 (2005).
61. K. A. McColl, W. Wang, B. Peng, R. Akbar, D. J. Short Gianotti, H. Lu, M. Pan, D. Entekhabi, Global characterization of surface soil moisture drydowns. *Geophys. Res. Lett.* **44**, 3682–3690 (2017).
62. P. J. Shellito, E. E. Small, B. Livneh, Controls on surface soil drying rates observed by SMAP and simulated by the Noah land surface model. *Hydrol. Earth Syst. Sci.* **22**, 1649–1663 (2018).
63. V. M. Muggeo, Segmented: An R package to fit regression models with broken-line relationships. *R News* **8**, 20–25 (2008).
64. P. E. McKight, J. Najab, Kruskal-wallis test, in *The Corsini Encyclopedia of Psychology* (2010), pp. 1. J. Wiley & Sons Inc., New York. <https://doi.org/10.1002/9780470479216.corpsy0491>.
65. M. Migliavacca, T. Musavi, M. D. Mahecha, J. A. Nelson, J. Knauer, D. D. Baldocchi, O. Perez-Priego, R. Christiansen, J. Peters, K. Anderson, M. Bahn, T. A. Black, P. D. Blanken, D. Bonal, N. Buchmann, S. Caldararu, A. Carrara, N. Carvalhais, A. Cescatti, J. Chen, J. Cleverly, E. Cremonese, A. R. Desai, T. S. El-Madany, M. M. Farella, M. Fernández-Martínez, G. Filippa, M. Forkel, M. Galvagno, U. Gomasaras, C. M. Gough, M. Goeckede, A. Ibrom, H. Ikawa, I. A. Janssens, M. Jung, J. Kattge, T. F. Keenan, A. Knohl, H. Kobayashi, G. Kraemer, B. E. Law, M. J. Liddell, X. Ma, I. Mammarella, D. Martini, C. Macfarlane, G. Matteucci, L. Montagnani, D. E. Pabon-Moreno, C. Panigada, D. Papale, E. Pendall, J. Penuelas, R. P. Phillips, P. B. Reich, M. Rossini, E. Rotenberg, R. L. Scott, C. Stahl, U. Weber, G. Wohlfahrt, S. Wolf, I. J. Wright, D. Yakir, S. Zaehle, M. Reichstein, The three major axes of terrestrial ecosystem function. *Nature* **598**, 468–472 (2021).
66. M. Jung, M. Reichstein, H. A. Margolis, A. Cescatti, A. D. Richardson, M. A. Arain, A. Arnett, C. Bernhofer, D. Bonal, J. Chen, D. Gianelle, N. Gobron, G. Kiely, W. Kutsch, G. Lasslop,

- B. E. Law, A. Lindroth, L. Merbold, L. Montagnani, E. J. Moors, D. Papale, M. Sottocornola, F. Vaccari, C. Williams, Global patterns of land-atmosphere fluxes of carbon dioxide, latent heat, and sensible heat derived from eddy covariance, satellite, and meteorological observations. *J. Geophys. Res. Biogeo.* **116**, G00J07 (2011).
67. T. E. Twine, W. Kustas, J. Norman, D. Cook, P. Houser, T. Meyers, J. Prueger, P. Starks, M. Wesely, Correcting eddy-covariance flux underestimates over a grassland. *Agric. For. Meteorol.* **103**, 279–300 (2000).
68. M. Migliavacca, M. Reichstein, A. D. Richardson, R. Colombo, M. A. Sutton, G. Lasslop, E. Tomelleri, G. Wohlfahrt, N. Carvalhais, A. Cescatti, M. D. Mahecha, L. Montagnani, D. Papale, S. Zaehle, A. Arain, A. Arneth, T. A. Black, A. Carrara, S. Dore, D. Gianelle, C. Helfter, D. Hollinger, W. L. Kutsch, P. M. Lafleur, Y. Nouvellon, C. Rebmann, H. R. Da Rocha, M. Rodeghiero, O. Roupsard, M.-T. Sebastià, G. Seufert, J.-F. Soussana, M. K. Van Der Molen, Semiempirical modeling of abiotic and biotic factors controlling ecosystem respiration across eddy covariance sites. *Glob. Chang. Biol.* **17**, 390–409 (2011).
69. C. R. Flechard, A. Ibrom, U. M. Skiba, W. de Vries, M. van Oijen, D. R. Cameron, N. B. Dise, J. F. Korhonen, N. Buchmann, A. Legout, D. Simpson, M. J. Sanz, M. Aubinet, D. Loustau, L. Montagnani, J. Neiryck, I. A. Janssens, M. Pihlatie, R. Kiese, J. Siemens, A.-J. Francez, J. Augustin, A. Varlagin, J. Olejnik, R. Juszczak, M. Aurela, D. Berveiller, B. H. Chojnicki, U. Dämmgen, N. Delapierre, V. Djuricic, J. Drewer, E. Dufrêne, W. Eugster, Y. Fauvel, D. Fowler, A. Frumau, A. Granier, P. Gross, Y. Hamon, C. Helfter, A. Hensen, L. Horváth, B. Kitzler, B. Kruijt, W. L. Kutsch, R. Lobo-do-Vale, A. Lohila, B. Longdoz, M. V. Marek, G. Matteucci, M. Mitasinkova, V. Moreaux, A. Neftel, J.-M. Ourcival, K. Pilegaard, G. Pita, F. Sanz, J. K. Schjoerring, M.-T. Sebastià, Y. S. Tang, H. Uggerud, M. Urbaniak, N. van Dijk, T. Vesala, S. Vedic, C. Vincke, T. Weidinger, S. Zechmeister-Boltenstern, K. Butterbach-Bahl, E. Nemitz, M. A. Sutton, Carbon–nitrogen interactions in European forests and semi-natural vegetation—Part 1: Fluxes and budgets of carbon, nitrogen and greenhouse gases from ecosystem monitoring and modelling. *Biogeosciences* **17**, 1583–1620 (2020).
70. AppEEARS Team. (2021). Application for Extracting and Exploring Analysis Ready Samples (AppEEARS). Ver. 2.67. NASA EOSDIS Land Processes Distributed Active Archive Center (LP DAAC), USGS/Earth Resources Observation and Science (EROS) Center, Sioux Falls, South Dakota, USA, <https://lpdaacsvc.cr.usgs.gov/appears> [accessed 28 December 2021].
71. R. Myneni, Y. Knyazikhin, T. Park, MOD15A2H MODIS/terra leaf area index. *FPAR 8-day L4 Global 500 m SIN Grid V006 Data Set* (2015).
72. L. Poggio, L. M. De Sousa, N. H. Batjes, G. Heuvelink, B. Kempen, E. Ribeiro, D. Rossiter, SoilGrids 2.0: Producing soil information for the globe with quantified spatial uncertainty. *Soil* **7**, 217–240 (2021).
73. Y. Huang, P. Ciais, M. Santoro, D. Makowski, J. Chave, D. Schepaschenko, R. Z. Abramoff, D. S. Goll, H. Yang, Y. Chen, W. Wei, S. Piao, A global map of root biomass across the world's forests. *Earth Syst. Sci. Data* **13**, 4263–4274 (2021).
74. J. K. Green, A. Ballantyne, R. Abramoff, P. Gentine, D. Makowski, P. Ciais, Surface temperatures reveal the patterns of vegetation water stress and their environmental drivers across the tropical Americas. *Glob. Chang. Biol.* **28**, 2940–2955 (2022).
75. J. H. Friedman, Greedy function approximation: A gradient boosting machine. *Ann. Statist.* **29**, 1189–1232 (2001).
76. J. Monteith, Evaporation and surface temperature. *Q. J. Roy. Meteorol. Soc.* **107**, 1–27 (1981).
77. S. Pennypacker, D. Baldocchi, Seeing the fields and forests: Application of surface-layer theory and flux-tower data to calculating vegetation canopy height. *Bound.-Layer Meteorol.* **158**, 165–182 (2016).
78. T. F. Keenan, D. Y. Hollinger, G. Bohrer, D. Dragoni, J. W. Munger, H. P. Schmid, A. D. Richardson, Increase in forest water-use efficiency as atmospheric carbon dioxide concentrations rise. *Nature* **499**, 324–327 (2013).

**Acknowledgments:** We would like to thank the ICOS Infrastructure for support in collecting and curating the eddy covariance data. This work used global eddy covariance data acquired and shared by the FLUXNET community, including these networks: AmeriFlux, AfriFlux, AsiaFlux, CarboAfrica, CarboEuropeIP, CarboItaly, CarboMont, ChinaFlux, Fluxnet-Canada, GreenGrass, ICOS, KoFlux, LBA, NECC, OzFlux-TERN, TCOS-Siberia, and USCCC. The ERA-Interim reanalysis data are provided by ECMWF and processed by LSCE. The FLUXNET eddy covariance data processing and harmonization were carried out by the European Fluxes Database Cluster, AmeriFlux Management Project, and Fluxdata project of FLUXNET, with the support of CDIAC and ICOS Ecosystem Thematic Center and the OzFlux, ChinaFlux, and AsiaFlux offices.

**Funding:** This work was financially supported by the European Research Council Synergy project SyG-2013-610028 IMBALANCE-P and the ANR CLAND Convergence Institute. Z.F. acknowledges support from the CNES (5100019800). I.C.P. acknowledges support by European Research Council funding under the European Union's Horizon 2020 research and innovation program (grant agreement no. 787203 REALM). I.C.P. and P.G. acknowledge support by the LEMONTREE (Land Ecosystem Models based On New Theory, observation and Experiments) project, funded through the generosity of E. Schmidt and W. Schmidt by recommendation of the Schmidt Futures program. **Author contributions:** Z.F. and P.C. designed the study. Z.F. performed the analysis. Z.F. and P.C. wrote the paper with the inputs from all co-authors. A.F.F., I.C.P., P.G., J.-P.W., D.M., P.C.S., and A.B. provided methodological suggestions and contributed to the interpretation of the results. **Competing interests:** The authors declare that they have no competing interests. **Data and materials availability:** All data needed to evaluate the conclusions in the paper are present in the paper and/or the Supplementary Materials. The eddy covariance measurements are obtained from the ICOS (<https://doi.org/10.18160/2G60-ZHAK>), AmeriFlux (<https://ameriflux.lbl.gov/>), and FLUXNET2015 datasets (<https://fluxnet.fluxdata.org/data/fluxnet2015-dataset/>).

Submitted 4 May 2022  
Accepted 19 September 2022  
Published 4 November 2022  
10.1126/sciadv.abq7827



## Critical soil moisture thresholds of plant water stress in terrestrial ecosystems

Zheng Fu, Philippe Ciais, Andrew F. Feldman, Pierre Gentine, David Makowski, I. Colin Prentice, Paul C. Stoy, Ana Bastos, and Jean-Pierre Wigneron

*Sci. Adv.*, **8** (44), eabq7827.  
DOI: 10.1126/sciadv.abq7827

### View the article online

<https://www.science.org/doi/10.1126/sciadv.abq7827>

### Permissions

<https://www.science.org/help/reprints-and-permissions>

Use of this article is subject to the [Terms of service](#)